Journal of Magnetic Resonance **140,** 41–57 (1999)
Article ID jmre.1999.1821, available online at http://www.idealibrary.com on IDEAL®

High-Resolution Strain Analysis of the Human Heart with Fast-DENSE

Anthony H. Aletras, Robert S. Balaban, and Han Wen

Laboratory of Cardiac Energetics, NHLBI, NIH, Bethesda, Maryland 20892

Received March 10, 1999; revised May 10, 1999

Single breath-hold displacement data from the human heart were acquired with fast-DENSE (fast displacement encoding with stimulated echoes) during systolic contraction at 2.5 × 2.5 mm in-plane resolution. Encoding strengths of 0.86–1.60 mm/π were utilized in order to extend the dynamic range of the phase measurements and minimize effects of physiologic and instrument noise. The noise level in strain measurements for both contraction and dilation corresponded to a strain value of 2.8%. In the human heart, strain analysis has sufficient resolution to reveal transmural variation across the left ventricular wall. Data processing required minimal user intervention and provided a rapid quantitative feedback. The intrinsic temporal integration of fast-DENSE achieves high accuracy at the expense of temporal resolution.

Key Words: **cardiac; function; DENSE; STEAM; tagging; phase contrast; stimulated echoes; fast-DENSE; heart; PC; stimulated echo.**

INTRODUCTION

Cardiac MRI has seen tremendous growth during the past few years. Technological advancements in both the software and the hardware of commercially available MR scanners have allowed for faster data acquisition as well as improved image quality from EKG-gated single breath-hold exams in humans. Moreover, the same technology allows current research to also focus on obtaining data without breath-holding the patient. The major questions that need to be addressed in a cardiac evaluation diagnostic exam are usually associated with heart anatomy, tissue metabolism, perfusion, and function. Faster and more robust imaging methods make MR cardiac exams good candidates for both diagnosis and screening.

Myocardial function is one of the areas where cardiac MR is superior to other imaging modalities. Experiments involving myocardial tagging have already been implemented with success during the past few years. Regional functional data in 2D and 3D have been the focus of such experiments (*1–5*). Recently, the processing and interpretation of time-course 3D data sets have added to the understanding of how the heart behaves under abnormal electrical conduction and ectopic beat generation (*6*). However, techniques involving regional myocardial strain evaluation with tagging lack high spatial resolution since they require clear tag-grid definition. Tagging also entails significant data processing effort on behalf of the user. Tagging grid identification remains one of the major hurdles of this methodology despite attempts to automate the process of grid tracking (*7*).

Magnetic resonance phase contrast (PC) velocity encoding of the myocardial wall (*8–13*) can provide functional information at high spatial resolution. Data processing with PC data is easily performed since velocity information is directly extractable from the complex digitized signal. Bulk motion and rotation correction via postprocessing (*14*) can allow for data visualization with minimal user effort. However, PC velocity-encoding techniques sample the first derivative of displacement with respect to time and therefore signal-to-noise ratio can be a limiting factor when considering strain-rate calculations. Integration of time-course PC velocity data has allowed for strain estimation (*11*) but image registration complicates data processing and introduces error in the strain estimates.

Displacement encoding with stimulated echoes (DENSE), a novel method in cardiac MRI based on work by Reese *et al.* (*13*), was previously demonstrated in canines *in vivo* (*16*). DENSE encodes displacement onto the phase of the spin during the mixing time TM of a STEAM experiment. As such, extracting displacement information from the phase images is similar to PC velocity-encoding methods. The measured displacement has sufficient precision for accurate strain calculations. Data processing involves little operator interaction. In our original work, data from the canine heart were collected in a 4T whole-body magnet at one *k*-space line per respiratory cycle. To acquire 2D mechanical strain data for humans with this technique, the scan would require approximately 15 min per slice.

In this work we present initial 2D functional data from the human heart acquired with a multishot segmented *k*-space EPI sampling scheme we call fast-DENSE. Fast-DENSE collects a single-slice 2D data set in one breath-hold. The signal-to-noise ratio in these displacement data sets allowed for transmural mechanical strain analysis at relatively high spatial resolution.

METHODS

All experiments were performed on a dedicated cardiovascular 1.5-T Signa LX2 MR scanner (General Electric Medical Systems, Milwaukee, WI). The system was fitted with a three-

1090-7807/99

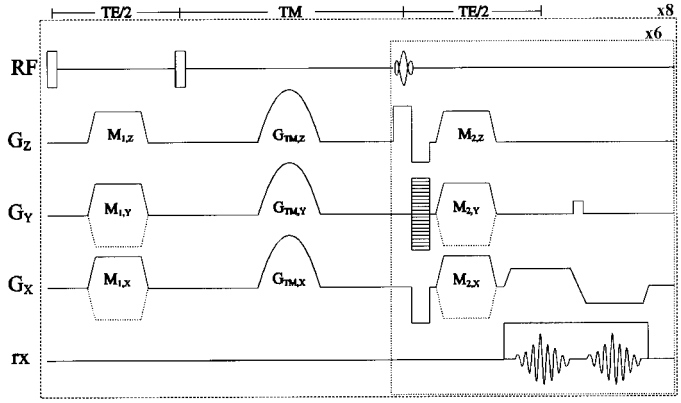

FIG. 1. Fast-DENSE pulse sequence timing diagram.

axis body gradient coil set capable of 23 mT/m in double oblique planes at slew rates up to 150 T/m/s. The receive-only phased array supplied with the system was utilized for signal detection. This consisted of two anterior and two posterior surface coils, each sampled through an independent receiver.

The stimulated echo experiment consisted of a 90° RF excitation pulse followed by position encoding. This was accomplished by means of gradient pulses during the first half of TE (Fig. 1) at up to 0.86 mm per π radians (net gradient moment of $M_1 = 13{,}680$ μs*mT/m). The phase accumulated at a location r_1 in space was

$$\varphi(r_1) = \gamma M_1 r_1.$$

Following the second 90° RF pulse, the encoded spins were then preserved for approximately 100 ms along the longitudinal axis. During this period of time (TM), cardiac motion displaced the phase-tagged myocardial voxels to a different position r_2. The position-encoded magnetization was recalled via a train of small flip angle RF pulses onto the transverse plane as described later. There, during this second half of TE, a gradient moment $M_2 = M_1$ imparted phase to the spins according to

$$\varphi(r_2) = \gamma M_2 r_2.$$

Thus, the measured residual phase for spins that moved at this new location r_2 during TM was

$$\varphi_{\mathrm{RES}} = \gamma M_1 r_1 - \gamma M_2 r_2 = \gamma M_1 \Delta r.$$

In the original paper (*16*), to ensure that the residual phase observed was accumulated only as a result of the displacement encoding, a reference scan with $M_1 = M_2 = 0$ was subtracted from the encoded data set. The actual implementation of the reference scan with fast-DENSE was revised to include part of the encoding moments (Fig. 1) as discussed later. In both scans, it was necessary to adequately suppress signal arising from magnetization that had relaxed during TM. These were spins that did not pertain to the stimulated echo. Therefore, in both scans, an additional gradient moment of 6500 μs*mT/m along the slice-encoding direction was added during the two halves of TE. Crushing the FID signal with a gradient pulse along the slice direction was deemed necessary since this direction is the most effective for this purpose. The observed signal for a pixel is the combined signal from the spins contained in the pixel integrated along all three directions. Since each pixel has its longest dimension along the slice-encoding direction, less gradient power is required along the slice in order to adequately dephase unwanted signal contributions such as the FID. Since this crusher pulse was applied in both the encoded and the reference scan, phase shifts due to displacement along the slice direction were zeroed out in the DENSE data set.

Recalling the position-encoded prepared magnetization onto the transverse plane via a train of small flip angle RF pulses allowed for several lines of *k*-space to be acquired from a single STEAM preparation. For each RF pulse, a portion of the position-encoded M_Z magnetization was recalled onto the transverse plane and subsequently was displacement-encoded via the second gradient moment, M_2 (Fig. 1). For each of these RF shots, following the application of M_2, two gradient echoes were formed and acquired. Thus, two lines of *k*-space were filled for each RF pulse. (Acquiring data at longer echo trains was considered but it always resulted in poor image quality and reduced signal-to-noise ratios.) Subsequent RF pulses recalled the remaining M_Z magnetization. A total of six 30° RF pulses were utilized to encode 12 lines of *k*-space from a single STEAM preparation. A typical experiment had a matrix size of 128×96 that corresponded to a rectangular FOV. Therefore, each image was acquired in eight segments at one segment per heartbeat, triggered by the EKG signal. For 2D fast-DENSE data three images were collected, i.e., X-encoded, Y-encoded, and the reference. As such, a complete 2D data set was collected in 24 heartbeats within a single breath-hold. The effective echo time was 4.7 ms and points were sampled at a bandwidth of 62 kHz. The TR between RF shots was 4.3 ms.

Since each of the images was collected in eight EKG-triggered segments, a modification of the segmented centric *k*-space-encoding scheme was utilized to minimize the effective echo time. In addition, this modified centric scheme provided smooth transitions in *k*-space. Out of the two gradient-recalled echoes formed following each RF shot, the first was assigned to the central half of *k*-space. As such, the central 48 *k*-space lines were filled with echoes of 4.7 ms echo time. Since a train of six RF shots was utilized for each of the eight segments, these 48 lines were arranged in six groups. Each group consisted of eight echoes that corresponded to the same RF shot in the RF trains of the eight segments. The echo groups corresponding to earlier RF shots in the train were positioned

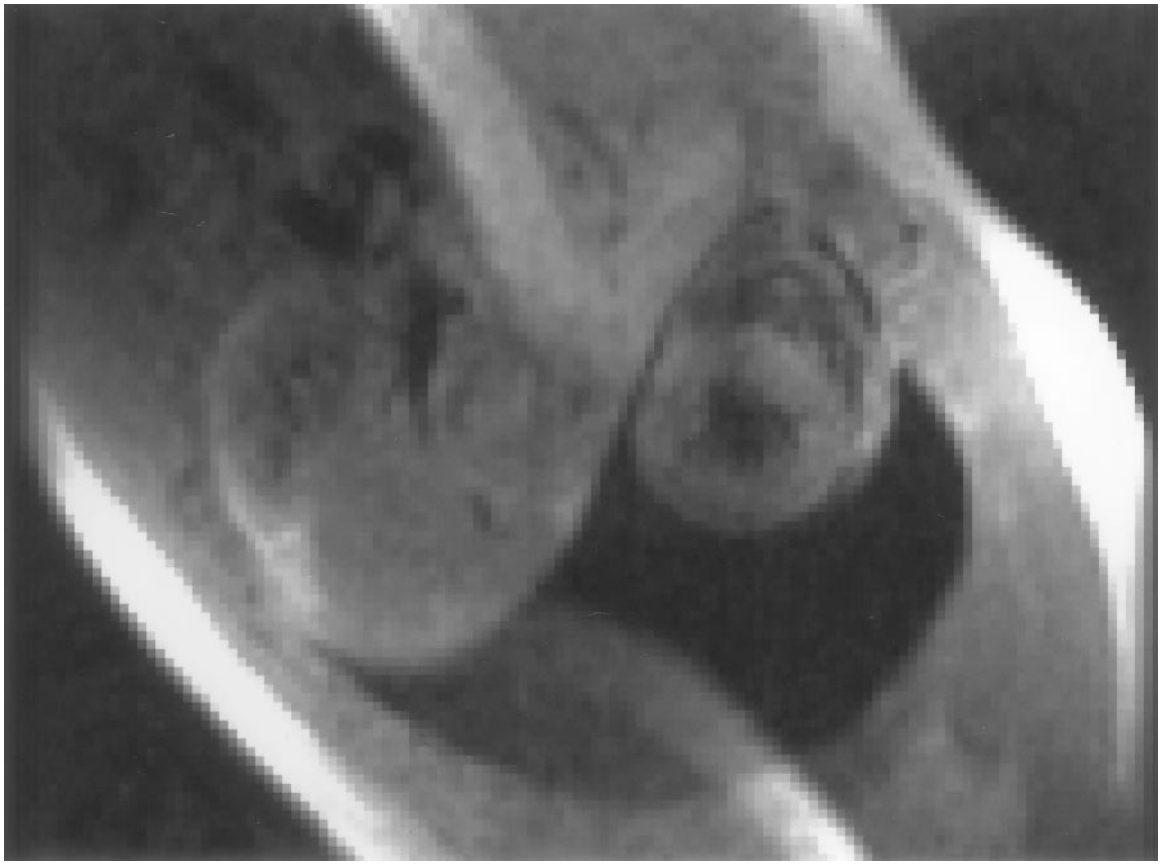

FIG. 2. Short-axis magnitude image of the human heart acquired with fast-DENSE.

closer to the center of *k*-space. The outer half of *k*-space was filled with the second echo of each RF shot in a similar manner.

Short-axis multislice displacement data from six normal volunteers (five males, one female, ages 25 to 42) were collected with fast-DENSE. Since nonselective RF pulses were utilized to store the magnetization along the longitudinal axis, each slice required a separate breath-hold. Displacement encoding was performed as previously described at up to 0.86 mm/π. With rectangular FOV, the pixel size was 2.5×2.5 mm for a slice thickness of 7 mm. The selected slice thickness was determined experimentally. Thicker slices sometimes resulted in severe signal loss due to intravoxel dephasing whereas thinner ones resulted in unacceptable SNR. Displacement was recorded with DENSE over the last 100 ms of systole. A user-programmable delay allowed for accurate positioning of the encoding period. The onset of the encoding period was approximately 230 ms from the QRS complex. This delay was volunteer dependent and was determined from a cine loop that was acquired subsequent to the localizing scans. As such, imaging was performed at end-systole.

Processing of raw *k*-space data was done with custom written programs in IDL (Research Systems Inc., Boulder, CO). Phase map differences were constructed from the reference scan and each of the encoded images (*17*). Following manual myocardial border segmentation, the maps were phase-unwrapped and scaled to the position-encoding gradient strength, yielding separate displacement maps for the X and Y directions. The combination of the 1D displacement maps produced 2D displacement arrow plots as described under Results. The deformation of each square of four neighboring pixels was dissociated into a rotation and two principle directions of strain (*18*) via eigenvector and eigenvalue computations. The principal strain directions were plotted with color coding that reflected the percentage of strain. Two color maps were created. The first charted the principal direction of contraction and therefore contained only eigenvectors with eigenvalues smaller than 1.0. Similarly, the second displayed the principal direction of myocardial dilation. A rotation map, which describes how tissue depicted by four neighboring pixels twists from its original orientation, was also computed via this analysis method. The average value of rotation was reported. Typical data processing time for a DENSE set was less than 1 min on a Pentium 200-MHz computer. This time included user interaction with the software.

In order to determine the noise level and to separate instrument-generated noise from measurement errors that were induced by physiological motion, experiments were performed in phantoms and *in vivo.* Multislice data from a stationary agar

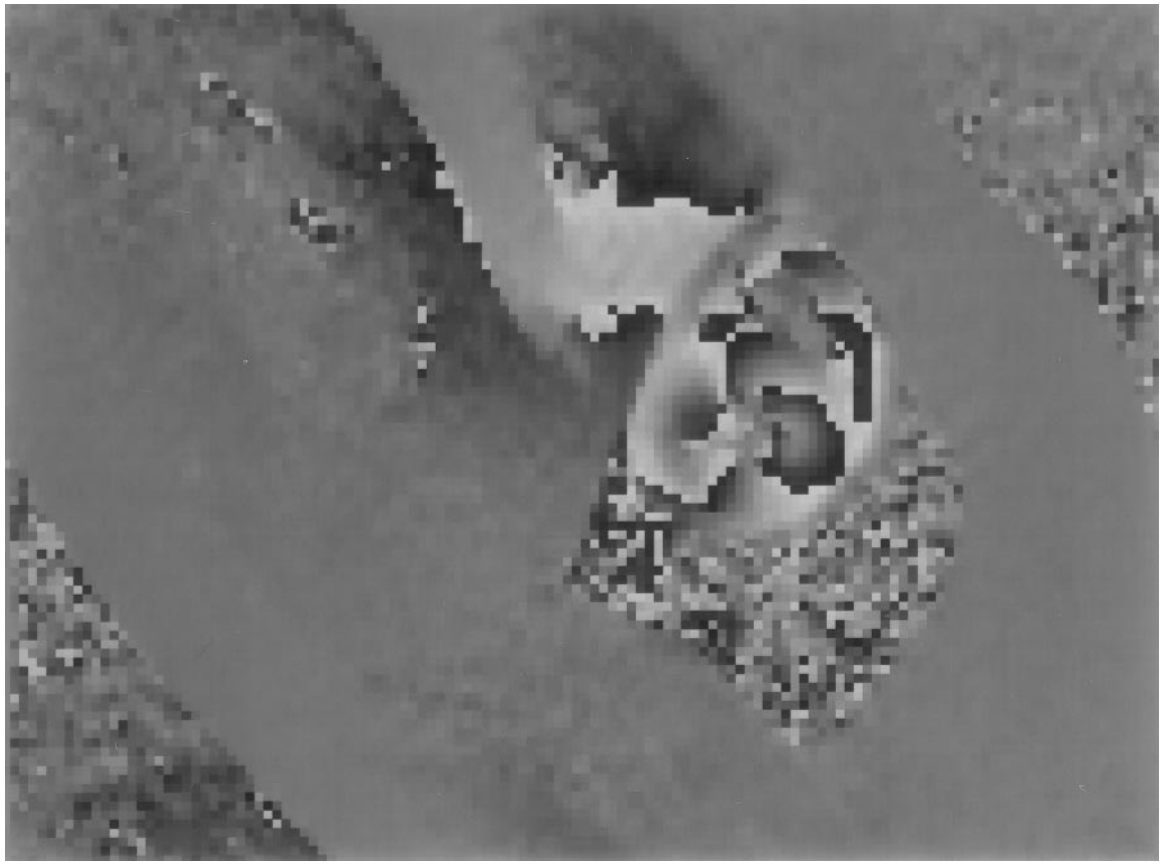

FIG. 3. X displacement phase map of the human heart over the last 105 ms of systole. Range is $\pm 180°$.

phantom, positioned at the location in the scanner where the heart is usually present, were collected with fast-DENSE parameters identical to those applied for the human experiments. These served to map and quantify spatially dependent phase errors induced by eddy currents and Maxwell terms. In this manner, instrument-generated systematic noise was quantified.

To verify displacement measurement accuracy, data were also acquired from a rotating cylindrical agar phantom (8-cm diameter, rotating at 34.3 revolutions per minute). These data sets also served as the means for evaluating software performance. As previously described, since the imaging part of fast-DENSE persists for 50 ms, phantom rotation of 10.28° occurs during that period of time. Due to this constant and high angular velocity of the phantom, axial images exhibited severe motion artifacts that were not present in the human data sets. To counter this effect, the DENSE phantom data were collected in 48 segments. For each segment, one RF shot was applied and two gradient-recalled echoes were acquired. This limited the imaging portion of the sequence to 4.5 ms, which was sufficient to eliminate motion artifacts. As expected, image acquisition was prolonged by a factor of 6 when compared to the *in vivo* case. This artifact constraint was not present in the human heart since the rotational component, over 50 ms in end-systole, is at least an order of magnitude smaller than that observed in phantom experiments and as a result does not manifest as a problem. Pixel size for the phantom data was set at 1.5×1.5 mm. DENSE encoding was set at 0.86 mm per π radians. Average rotation and strain were computed for the rotating phantom and compared with the known rate of rotation. Since acquisition parameters for these experiments are not identical to the ones used for human exams, the data from the rotating phantom merely served to verify that both the pulse sequence calibration and the data processing software were functioning as expected. Any other comparison with respect to SNR values and artifacts would not be valid.

Total noise quantification in humans was considered to be of particular importance for DENSE measurements. Besides random noise, other sources of phase errors are motion inside an inhomogeneous static field during TM and timing jitter introduced by physiological heart rate and EKG trigger variations. *In vivo* control data sets were collected in order to measure the overall noise level in DENSE experiments. In these data sets, instead of acquiring the reference along with X- and Y-encoded complex images, all three images had the same encoding gradients. To cover all cases, three control data sets were collected with gradients corresponding to X, Y, and reference-encoding strengths. Therefore, these control data sets yield maps that reflect the noise of the measurement between three

FIG. 4. Y displacement phase map of the human heart over the last 105 ms of systole. Range is ±180°.

scans with identical acquisition parameters. If no noise was present then such maps would show zero displacement. The control scans had net gradient moments along the X-, Y-, and Z-axes identical to those used for the *in vivo* experiments. Strain computation on these control sets provides quantitative estimates of the noise that is present in the *in vivo* strain maps of the human heart. To ensure that this is an accurate estimation of the total noise level of the *in vivo* results, experimental parameters were set as previously described except for the aforementioned difference in the encoding scheme. Once the total noise level had been determined, repeated DENSE data acquisition from the same location was performed in order to verify the reproducibility of the experiment.

RESULTS

Typical short-axis magnitude data from the apex of the human heart are shown in Fig. 2 (male, age 25, weight 88 kg). The center of this slice was prescribed 4 mm below the base of the papillary muscles. The phase maps that depict X and Y displacement are shown in Figs. 3 and 4. Note the multiple cycle wrapping of the phase over the FOV that is accomplished by 0.86 mm/π encoding. The corresponding 2D displacement arrow plot is displayed in Fig. 5. The computed strain maps are

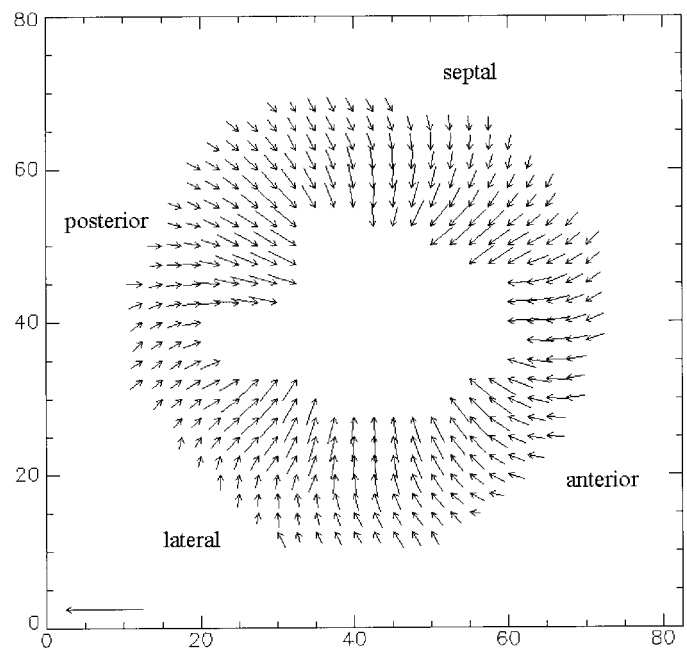

FIG. 5. 2D displacement arrow plot of the human heart (in mm) over the last 105 ms of systole computed from the X and Y displacement phase maps shown in Figs. 3 and 4. The horizontal arrow at the bottom left is 10 mm long.

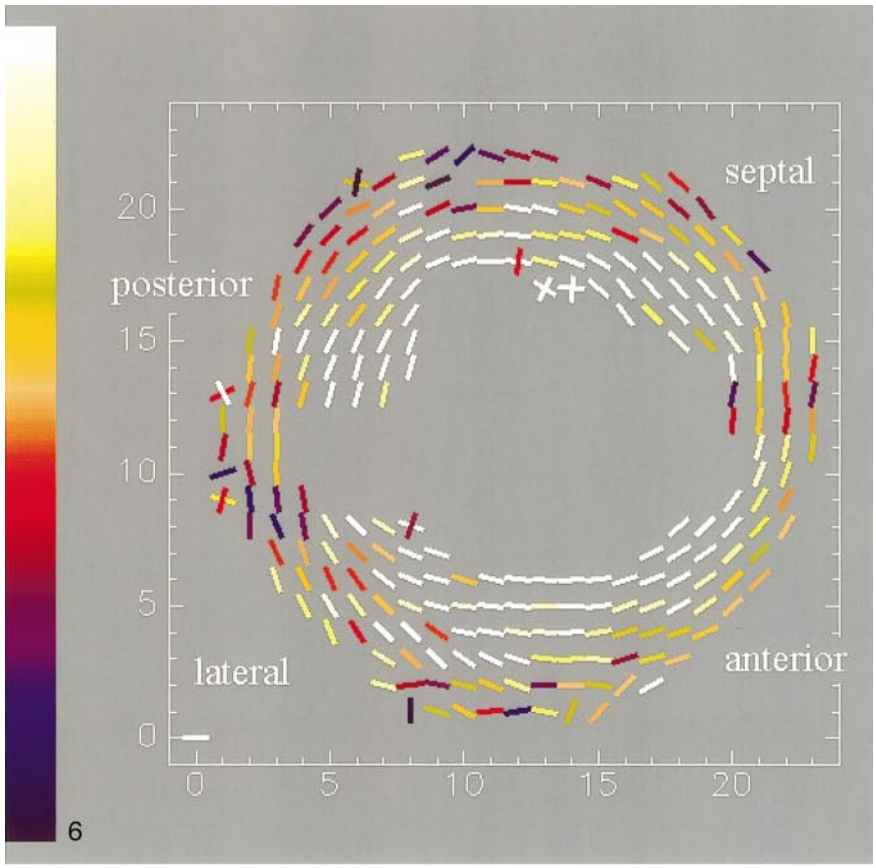
septal
posterior
lateral
anterior
0
5
10
15
20
6

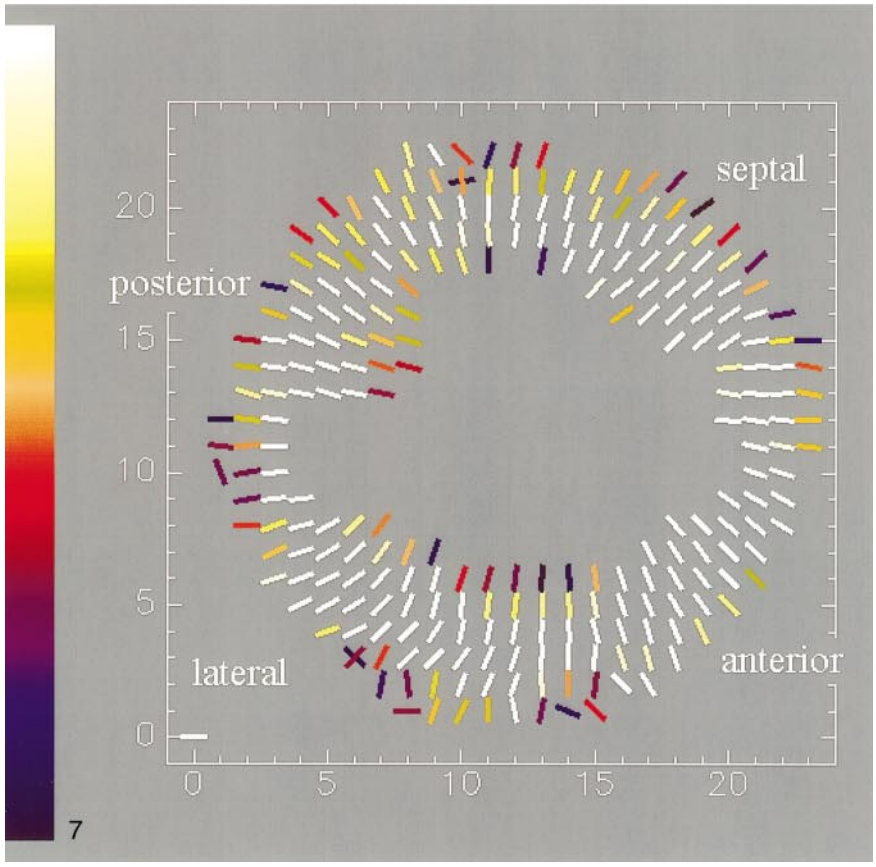
septal
posterior
lateral
anterior
0
5
10
15
20
7

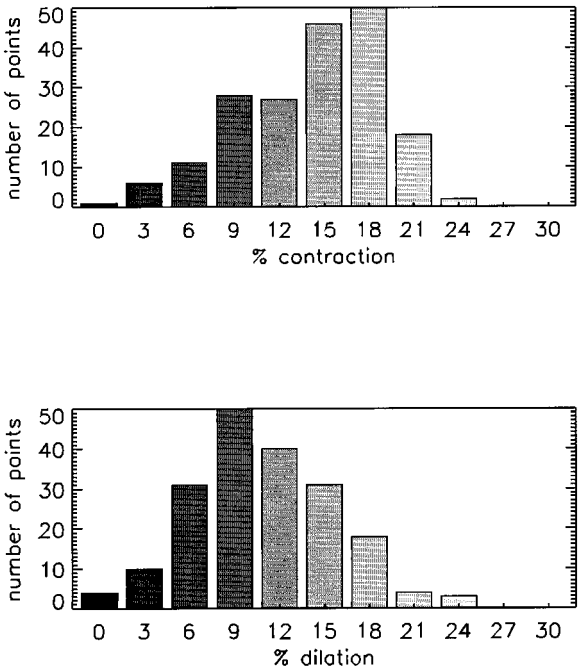

FIG. 8. Distribution of percentage dilation and shortening among the myocardial pixels. Data were obtained from a typical 25-year-old male volunteer (88 kg) with fast-DENSE. Histogram bin size is 3% strain.

presented as pairs of contraction and dilation in Figs. 6 and 7. The contraction maps depict the eigenvectors associated with the eigenvalues smaller than 1.0 with colored bars. The color represents the deviation of the magnitude of the corresponding eigenvalue from 1.0. Similarly, the dilation strain maps show the eigenvectors with eigenvalues greater than 1.0. Note that contraction occurs in a circumferential direction while dilation is radial. Furthermore, the endocardial strain is higher than the epicardial strain, as expected. The distribution of strain in the myocardium of a typical volunteer is shown in Fig. 8.

Stationary phantom data yield information with respect to instrument-generated noise. The phase map differences between each of the encoded directions minus the reference scan are presented in Figs. 9 and 10 for X and Y displacement, respectively. A range of ± 20 degrees around zero is shown. The corresponding average phase over the total area of the phantom was 0.012 (SD = 1.4) and 0.15 (SD = 1.4) degrees for X and Y displacements, respectively. As a result of the high encoding strength, these translate to 0.008-mm uncertainty in displacement measurements. No spatially dependent phase gradients were observed. The computed strain was 0.2% (SD = 0.2%) for both contraction and dilation. The calculated overall average rotation was 0.001° (SD = 0.1).

Displacement measurement accuracy was determined via rotating phantom experiments. The displacement arrow plot is shown in Fig. 11. Each arrowhead points to a pixel in the phantom depicted in the magnitude image. An arrow tail represents the initial position of a given pixel 50 ms earlier. This position was calculated as previously described. The data void observed in Fig. 11 is caused by an empty tube positioned parallel to the rotational axis, inside the agar phantom. This signal void could act as a displacement marker to measure rotational speed with conventional imaging methods. The primary directions of contraction and dilation are shown in Figs. 12 and 13, respectively. The ceiling for this display is set for strain of 2%. Since the agar phantom was rotating at a constant speed and had neither contraction nor dilation associated with it, these plots represent the noise level introduced by the instrument in the strain calculation measurements. This is true only for the given set of acquisition parameters. The noise is 0.5 and 0.6% strain for contraction and dilation, respectively. The average rotation calculated from the data set was 10.54° (SD = 0.36). This matches the actual rotation of the phantom over the encoding period, which was set to 10.28°. The calculated average rotation deviates from the actual rotation by 0.26°. The jitter introduced in the phantom's rotation by the mechanical coupling between the motor and the agar container is probably responsible for this deviation.

Total noise data in two humans were collected by using the same encoding gradients for all three images in a DENSE data set as described under Methods. The highest noise level occurred when all three images had encoding strength that corresponded to Y encoding. The phase maps that would correspond to X and Y displacement for a normal DENSE set are shown in Figs. 14 and 15, respectively. Strain computation yielded the contraction and dilation maps presented in Figs. 16 and 17, respectively. The principal directions of contraction and dilation were largely random. The average values in the contraction and dilation maps were 2.8% (SD = 2.5%) and 2.9% (SD = 2.5%), respectively. These values represent the overall noise level in the actual human DENSE measurements. Increased noise is observed in DENSE strain measurements of the posterior wall of the heart (Figs. 16 and 17). The geometry of the RF receiver coils is such that image SNR is low in these areas.

DISCUSSION

DENSE data allowed for high spatial resolution strain estimation in the human heart. The overall noise level in strain maps computed via control experiments was less than 3%. In

FIG. 6. Contraction strain map of the human heart over the last 105 ms of systole corresponding to Fig. 5. The principal direction of contraction is shown via colored bars and is mainly circumferential. Color scale represents 0 to 20% contraction. Average strain is 11.5%.

FIG. 7. Dilation strain map of the human heart over the last 105 ms of systole corresponding to Fig. 5. The principal direction of dilation is shown via colored bars and is mainly radial. Color scale represents 0 to 20% dilation. Average strain is 13.4%.

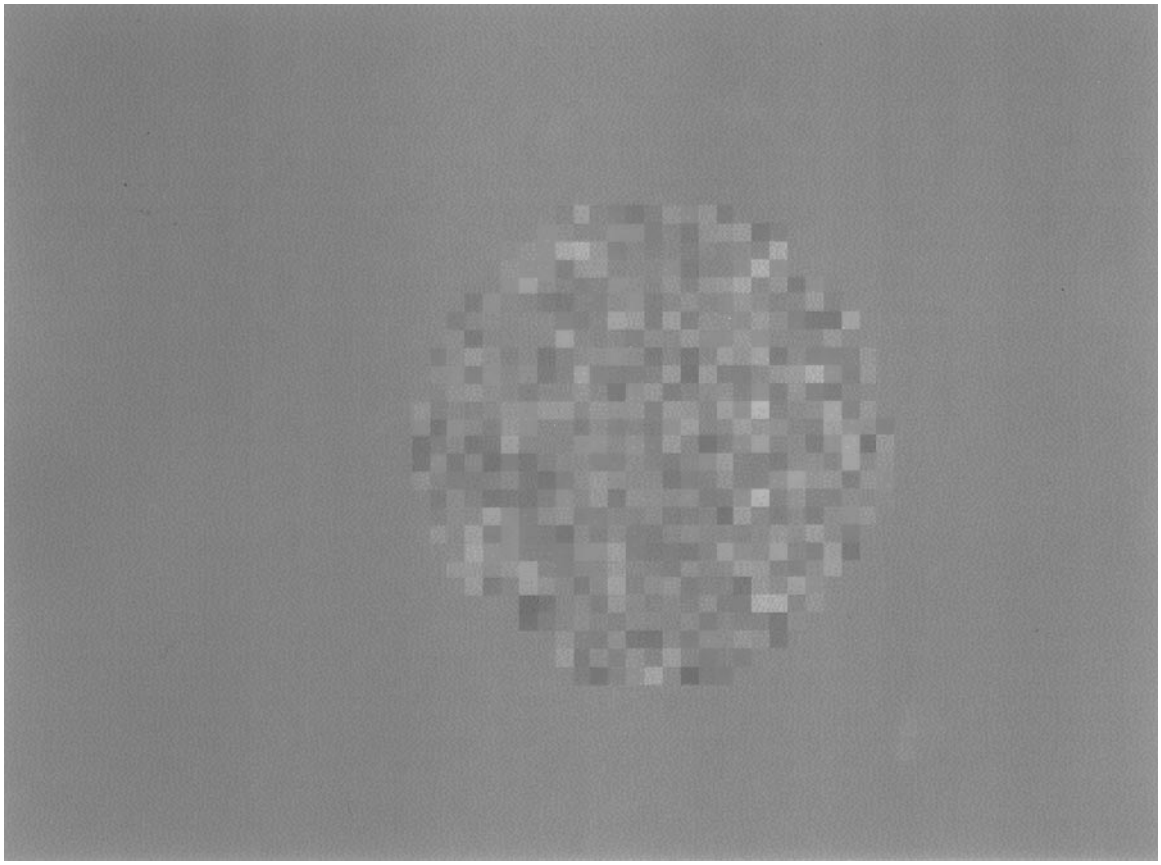

FIG. 9. X displacement phase map of the stationary phantom. Range is ±20°.

comparison, systematic noise due to eddy currents and Maxwell terms was evaluated to be negligible for the hardware used. Pulse sequence calibration and data processing software accuracy verification were demonstrated via rotating phantom experiments.

The main incentive for implementing DENSE in myocardial strain mapping is the extended phase dynamic range it provides by recording displacement over a long period of time and the associated insensitivity to both physiological and instrument-generated noise. These will be addressed in detail later along with other signal-to-noise ratio considerations. In addition, DENSE has several other features that make it a good candidate for cardiac functional imaging. First, black-blood contrast is an inherent property of images acquired with stimulated echoes at long TM periods (Fig. 2). The incoherent motion of blood during the displacement-encoding period results in severe intravoxel dephasing and subsequent signal loss. This type of image contrast is advantageous for separating the myocardium from the ventricular blood pool. Moreover, artifacts and phase contamination pertaining to blood motion are eliminated.

Another feature of fast-DENSE is the suppression of signal surrounding the heart. This eliminates sources of motion artifacts, especially from the chest wall areas proximal to the surface coil (Fig. 18). In the past, several approaches to limiting the FOV without aliasing artifacts have been proposed (*19, 20*). STEAM field of view localization can be easily implemented with DENSE by having the first two nonselective RF pulses converted to slab-selective along the X and Y directions. Even though the signal-to-noise ratio of the single breath-hold experiment is the limiting factor and does not allow for dramatic changes in FOV dimensions, this approach could prove to be useful in animal models where such time constraints are not present. In any case, suppressing the signal originating from the adipose tissue of the chest wall removes a potential source of motion-related artifacts.

An additional intrinsic feature of fast-DENSE is that displacement quantification is not susceptible to through-slice motion problems. In 2D cardiac functional imaging, with both tagging and phase methods, through-slice motion introduces error in the data. With this implementation of fast-DENSE, phase position-encoding during the STEAM preparation is done for the entire heart. This is accomplished via the two nonselective RF pulses of the preparation (Fig. 1). Since all the spins are phase-tagged, when the imaging RF train of selective pulses recalls longitudinal magnetization onto the transverse plane, it is guaranteed that the recalled spins will have already been encoded for position. As such, out-of-slice motion is not a concern for fast-DENSE.

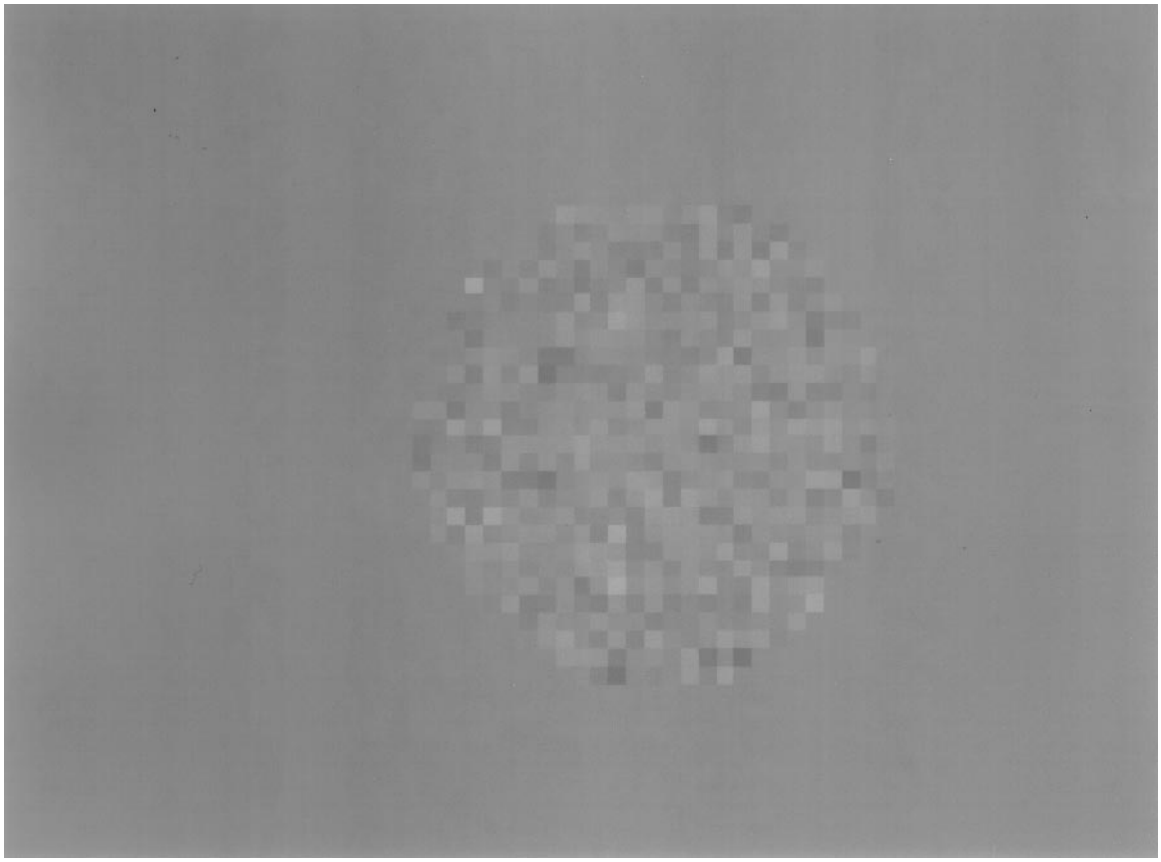

FIG. 10. Y displacement phase map of the stationary phantom. Range is ±20°.

The density of strain data that can be computed with fast-DENSE is only limited by pixel size. Since the phase of each pixel is modulated by displacement, strain data between neighboring pixels can be extracted. With the current implementation, 2D strain can be calculated for a voxel size of $2.5 \times 2.5 \times 7.0$ mm. This data density is superior to amplitude-modulated tagging methods and equivalent to that obtained by phase contrast velocity techniques. However, PC velocity measurements suffer from intrinsic SNR problems as will be discussed later.

Data processing of DENSE phase maps to yield displacement arrow plots is straightforward. Following phase subtraction from the reference scan, the X and Y displacement-encoded phase maps are combined and phase-unwrapped to create an arrow plot as previously described. The only interaction between the processing software and the operator is that of delineating the endocardial and epicardial borders. This task is facilitated by black-blood contrast. Local strain among neighboring pixels is computed within the defined myocardial area. If the displacement arrow plot is not required and only strain needs to be computed, then phase-unwrapping can be done at a local level. Thus, myocardial delineation is no longer necessary and as a result operator intervention can be elimi-

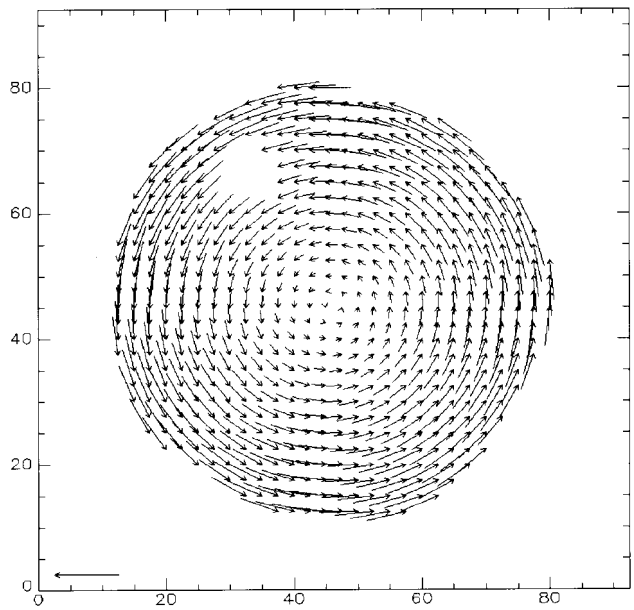

FIG. 11. 2D displacement arrow plot of the rotating phantom.

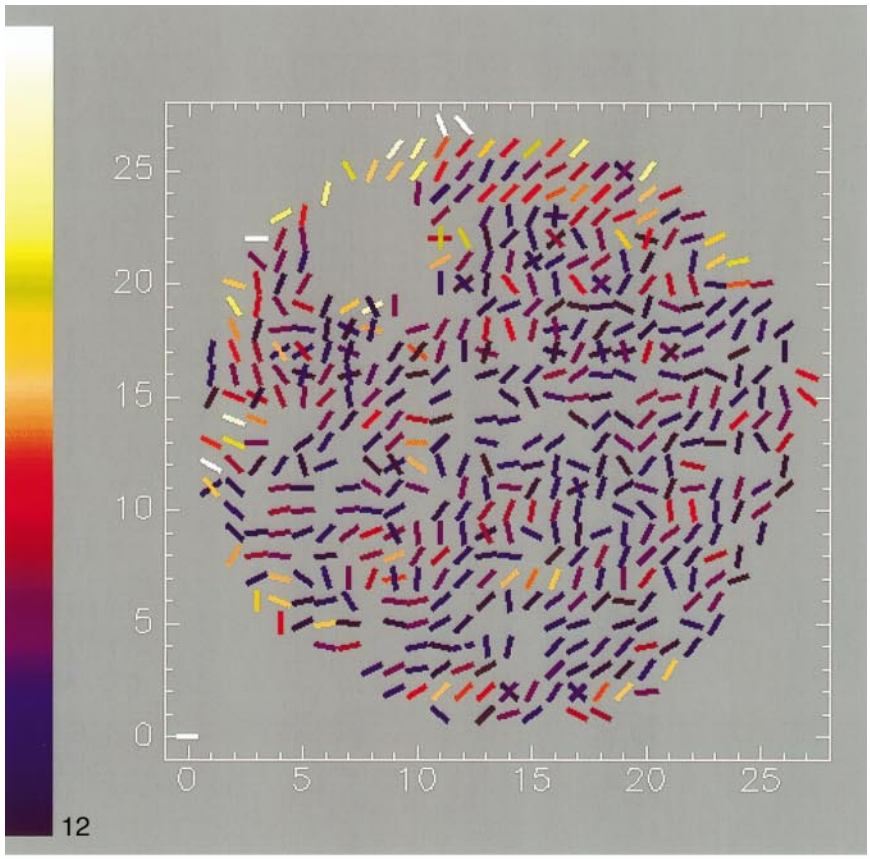
0
5
10
15
20
25
12

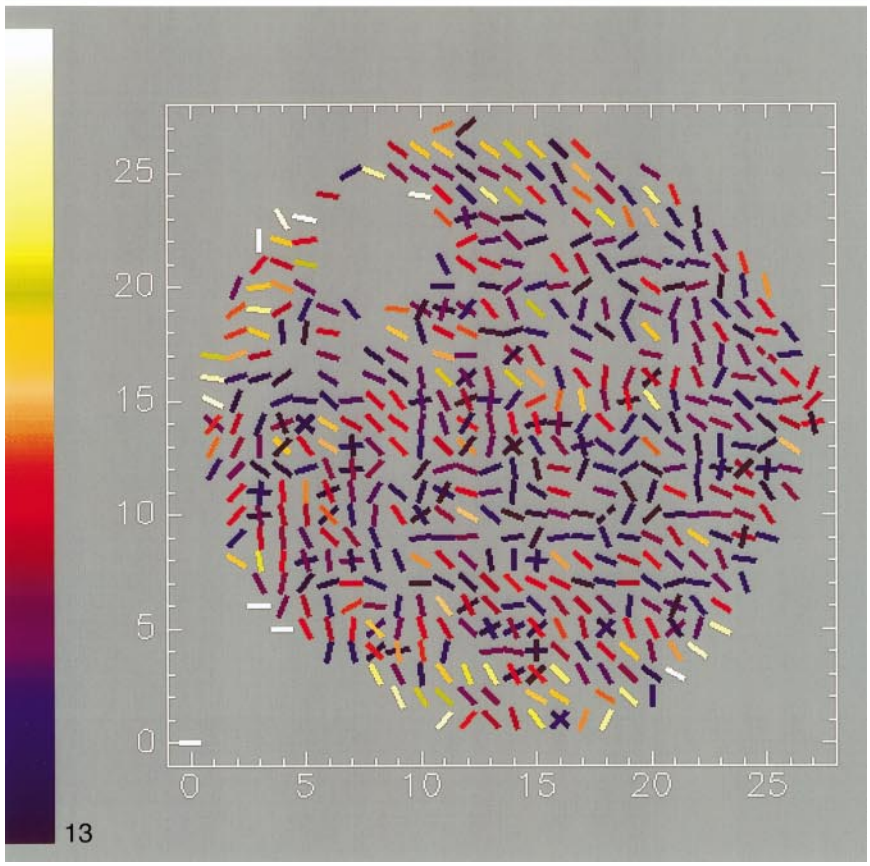
0
5
10
15
20
25
13

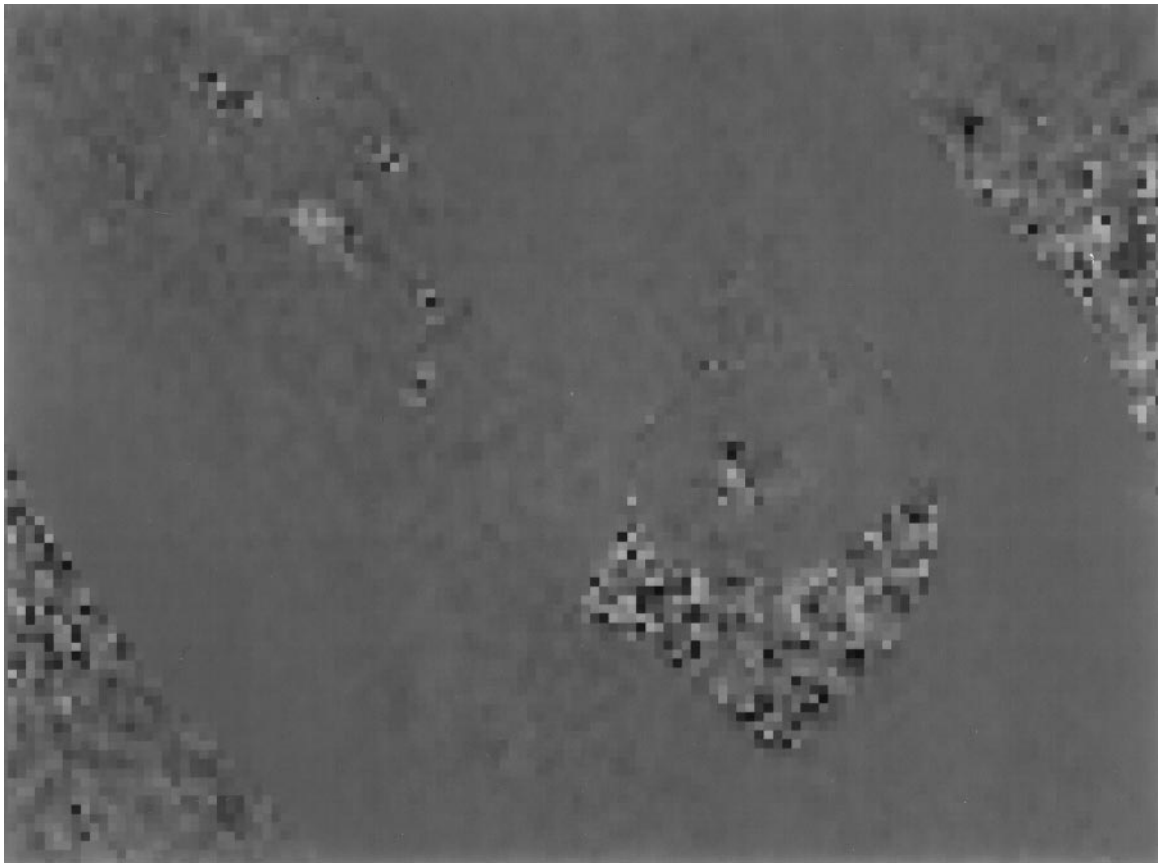

FIG. 14. X displacement phase map of the human heart over the last 105 ms of systole with X encoding substituted by an additional reference scan (see text). Grayscale range is ±20°.

nated all together. Therefore, data processing ease is one of the major advantages of DENSE.

DENSE displacement data can be considered as the time integral of PC velocity measurements over the TM period. The inherent process of integration results in phase maps with increased SNR and multiple-cycle phase-wrapping. At the same time, DENSE sacrifices temporal resolution for the same purpose. This can be partially compensated for by acquiring displacement data at different time points during systole with shorter encoding periods. However, in doing so, the aforementioned inherent advantages of DENSE are compromised. One has to weigh between temporal and spatial resolution to select a method suitable for a particular need.

In the future, gradient system performance could conceivably allow PC velocity techniques to acquire data free of phase artifacts induced by eddy currents and Maxwell terms. Furthermore, such technological advancements could potentially allow for faster data acquisition and eliminate other SNR problems that are discussed below. However, physiological limitations may ultimately limit the allowable gradient strength (*21*). Indeed, the first-order gradient moment required for PC velocity mapping to encode adequately for cardiac motion (0.1 m/s) without wrapping the phase multiple times across the field of view is approximately 3500 μs*G/cm. In order to increase SNR in PC velocity data, the phase will have to be wrapped and thus this moment will have to be increased to a level where peripheral nerve stimulation may be a concern.

Signal-to-noise ratio is of particular importance when considering cardiac functional methods that utilize information stored onto the phase of the spins. Not only is overall complex data SNR critical, but also any systematic source of phase noise can limit the scope of experiments performed via phase methods. Such sources of noise are eddy currents and Maxwell terms. A major goal of functional cardiac methods is precision

FIG. 12. Contraction strain map of the rotating phantom. The principal direction of contraction is shown via colored bars. Color scale represents 0 to 2% contraction. Average strain is 0.5% (SD = 0.5%).

FIG. 13. Dilation strain map of the rotating phantom. The principal direction of dilation is shown via colored bars. Color scale represents 0 to 2% contraction. Average strain is 0.6% (SD = 0.6%).

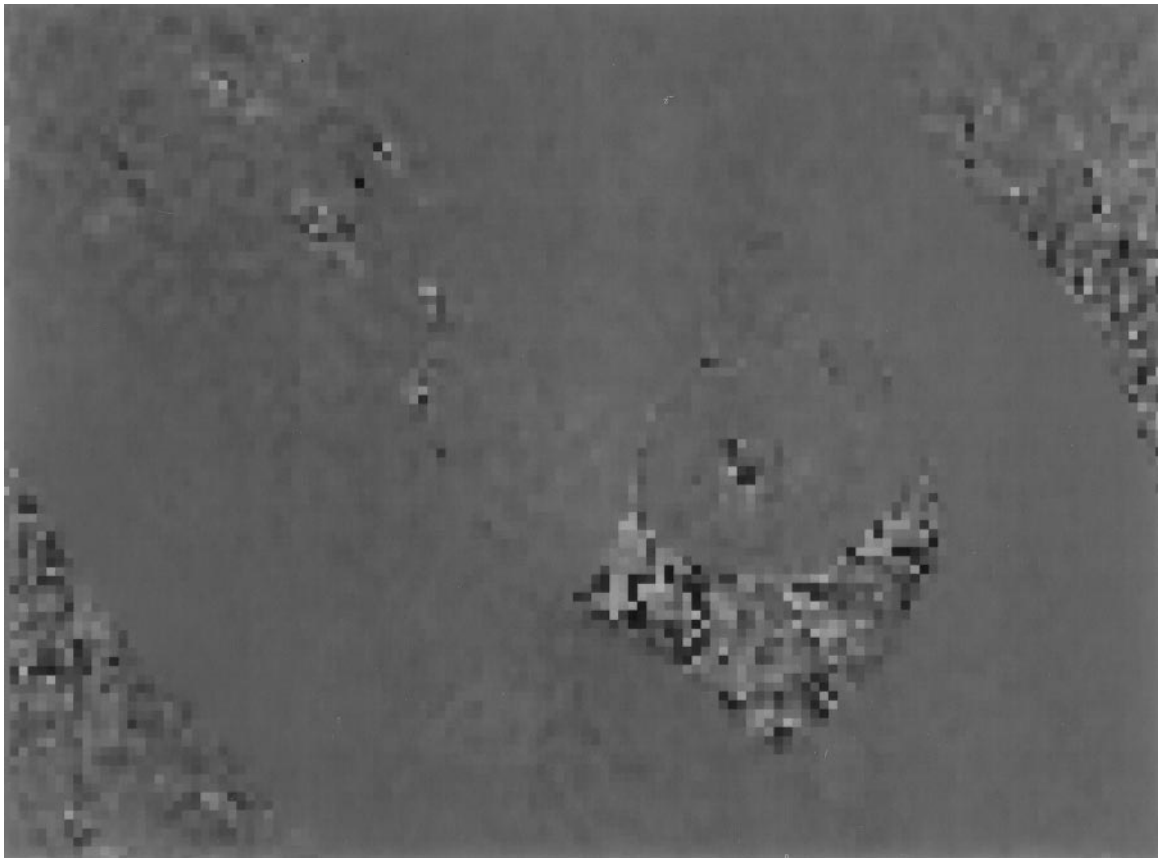

FIG. 15. Y displacement phase map of the human heart over the last 105 ms of systole with X encoding substituted by an additional reference scan (see text). Grayscale range is ±20°.

strain estimation, which is demanding on data SNR. Since differentiation is required to calculate mechanical strain among adjacent pixels, the SNR of the data has to be high. Therefore, care has to be exercised during data collection to ensure the SNR of the resulting strain maps.

Stimulated echoes have been applied to cardiac imaging with limited success in the past. One of the reasons is the inherent loss of 50% of the signal. Pioneering experiments in the human heart with STEAM by Frahm *et al.* (*22*) showed that other confounding factors for using stimulated echoes were scanner hardware performance in terms of RF coils and gradient system speed. Phased arrays and ultrafast gradient systems that are only limited by physiological constraints are now readily available. These technological advancements should lift the hardware barrier with respect to acquiring STEAM single breath-hold images at long TM encoding periods.

DENSE experiments are in some respects more demanding than single-shot STEAM imaging (*22*). In their original paper, Frahm *et al.* present data from the human myocardium at 4 ms TM. In addition, TE crushers along the slice direction alone crush the imaginary part of the signal. The selection of both parameters results in ample SNR for single-shot STEAM imaging since motion, contraction, and slice rotation are hardly an issue for such short TM periods. DENSE requires a prolonged encoding TM period and strong encoding TE gradient pulses in order to map displacement without compromising dynamic range and therefore data SNR. As such, both tissue deformation and slice rotation become important in determining the approach to be considered when sampling *k*-space. A segmented approach was found to be more favorable to single-shot gradient-recalled EPI imaging for these reasons. For each segment, a train of six RF pulses sampled the DENSE-prepared magnetization. For each RF pulse, two echoes were acquired. As described under Methods, the views corresponding to echoes with minimum TE and RF saturation were pushed toward the center of *k*-space. Therefore, echoes near the center of *k*-space suffered less from the depletion of M_z magnetization due to preceding RF shots. With the current readout scheme, there is a trade-off between SNR and speed. Since the ultimate goal is to create strain maps of the myocardium, one has to be cautious about how much SNR can be sacrificed for imaging speed. With fast-DENSE, the uncertainty introduced in strain measurements was 2.8% at 2.5 mm in-plane resolution. A higher noise level would likely decrease the usefulness of the strain data.

If the encoding gradient strength and duration along the three different axes are set too high (*23*), then rotation and tissue deformation due to contraction can result in additional signal loss (*24*). This is due to intravoxel dephasing. As such, the first-order moments of the gradients have to be adjusted carefully. Figure 19 shows an example where the encoding gradients along the slice direction caused such intravoxel dephasing in the free left ventricular wall. According to Fischer *et al.* (*23*), a signal drop of 20% should be expected as a result of tissue deformation. Slice rotation about an arbitrary axis that lies in the slice also results in a mismatch of the gradients bracketing the encoding period. However, it is estimated to be less than 1%. Such effect does not influence image quality for fast-DENSE.

It is interesting to note that theoretical signal loss due to tissue deformation in the presence of TE gradients along all three directions exists mostly as a result of the gradient pulses along the slice direction. This is true even when the moments utilized along all three directions are similar. The signal observed from a voxel is the integral of spins contained in it along all three dimensions. Gradient pulses during TE along the slice direction have the potential for degrading image quality more than any other. This is a direct manifestation of the voxel having its longest dimension along slice. A given phase dispersion per unit length will result in most efficient signal attenuation when integrated along the longest dimension of a voxel. For fast-DENSE, the first-order gradient moment required for encoding 0.86 mm/π along the X and Y directions is 1370 μs*G/cm. With the initial approach to DENSE (*16*) the encoding moment was solely applied to the X- and Y-encoded images. The displacement phase maps were constructed by subtracting the encoded images from a reference scan. The latter was acquired with a zero first-order moment along X and Y. With fast-DENSE the encoding moment was equally divided between the reference and the encoded scans with opposite polarities. This approach allowed for higher encoding moments without losing signal. Implementing high encoding moments diminishes the effect of systematic phase errors due to static field inhomogeneity, eddy currents, and Maxwell terms on the displacement measurements.

In several cases, regional signal loss was observed with TM at 100 ms. Increasing the encoding gradient pulses to values greater than 0.86 mm/π also caused signal dropout. The most severe signal loss was usually observed in areas of vigorous contraction. Similarly, at encoding strengths of 0.86 mm/π, signal loss occurred when the encoding period was prolonged to 350 ms in order to capture systole at its entirety. This signal loss was higher than T_1 effects alone would predict. Therefore, a trade-off between these two parameters has to be made. In essence, prolonging TM will result in more displacement to be captured and thus less encoding strength should be required to preserve the SNR at the same level. In some cases where regional contraction inhomogeneity exceeds the dynamic range that fast-DENSE can capture, it may be necessary to perform separate scans in order to measure strain with acceptable SNR. Another means for extending the dynamic range is by increasing the overall SNR of the image by utilizing imaging techniques, such as fast spin echo, that do not depend on recalling magnetization via low flip angle RF pulses.

Cardiac motion inside an inhomogeneous static field can provide yet another source for error when utilizing phase-based methods. B_0 inhomogeneity is a result of the plethora of tissue–air interfaces around the heart. In an ideal setting, when conducting phase experiments, the reference scan serves as a means for mapping every other source of phase accumulation except for the one that needs to be recorded. Subtraction of the reference scan from the encoded data set results in phase maps where only the desired contributions are present. However, this process can prove to be an additional source of error when considering a moving object. Unless the reference scan is acquired at exactly the same cardiac phase, the phase accumulated due to field inhomogeneity will not cancel out in the resulting phase map. This occurs because the heart is at a slightly different location for each of the two scans. There are two ways for minimizing errors originating from this process. Corresponding *k*-space lines of the two scans are either temporally spaced as close to one another as possible or acquired during successive heartbeats at the same cardiac phase. The first approach results in phase maps where a contribution of B_0 inhomogeneity is present. Depending on how steep the inhomogeneity gradient is and how much the heart has moved, phase maps can be significantly distorted. This is particularly true for PC velocity methods where motion over 1–2 ms gives relatively small phase contrast while the temporal spacing between the two scans (TR) is on the order of 20 ms. Arai *et al.* (*14*) have shown that such phase error can limit the applicability of PC velocity mapping in some parts of the heart.

Minimizing B_0 phase contributions by acquiring corresponding *k*-space lines of the reference and the encoded scan at the same cardiac phase of successive heartbeats has its own problems. The uncertainty introduced by EKG triggering, with respect to the actual point in time where a particular phase is acquired, can introduce phase errors comparable to the ones already mentioned. The corresponding *k*-space lines can be acquired as far apart as one TR interval for PC velocity methods. Thus, for velocity measurements, this approach is not any better than the one previously discussed due to the jitter introduced in the acquisition window by the prospective real-time EKG triggering. It is also worth noting that PC velocity pulse sequences utilize gradient echoes and therefore B_0 effects are strong. However, with DENSE the multiple heartbeat approach works quite well. Acquisition jitter introduced by EKG triggering is small when compared to the long encoding period. In addition, since the phase is wrapped multiple times over the field of view, B_0-induced phase errors be-

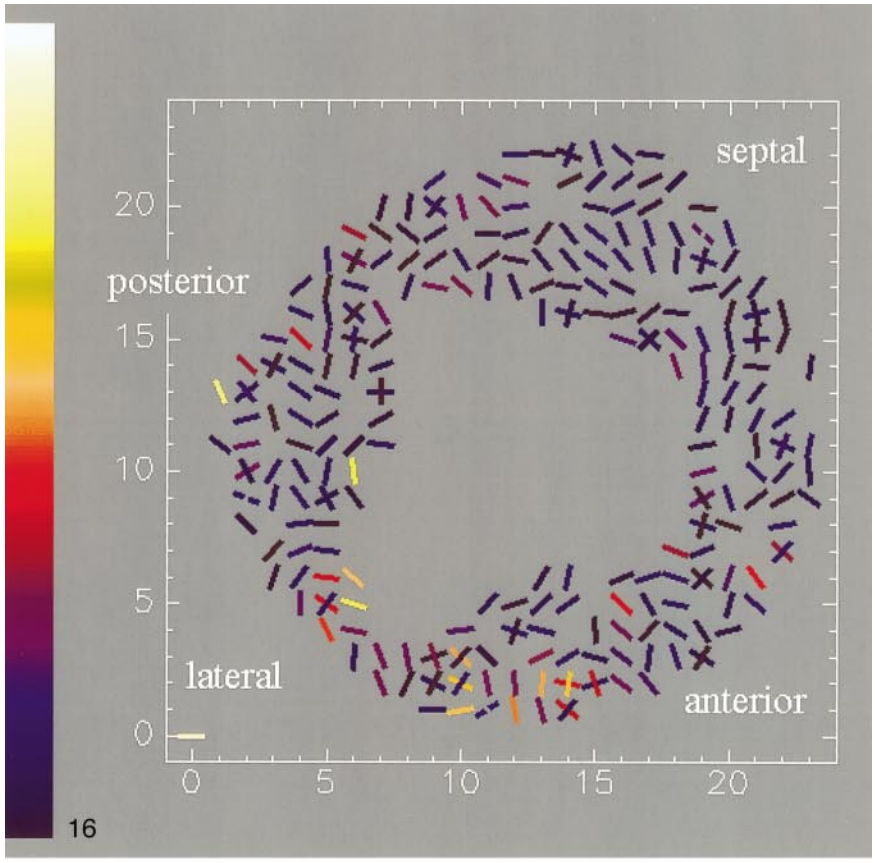
septal
posterior
lateral
anterior
0
5
10
15
20
16

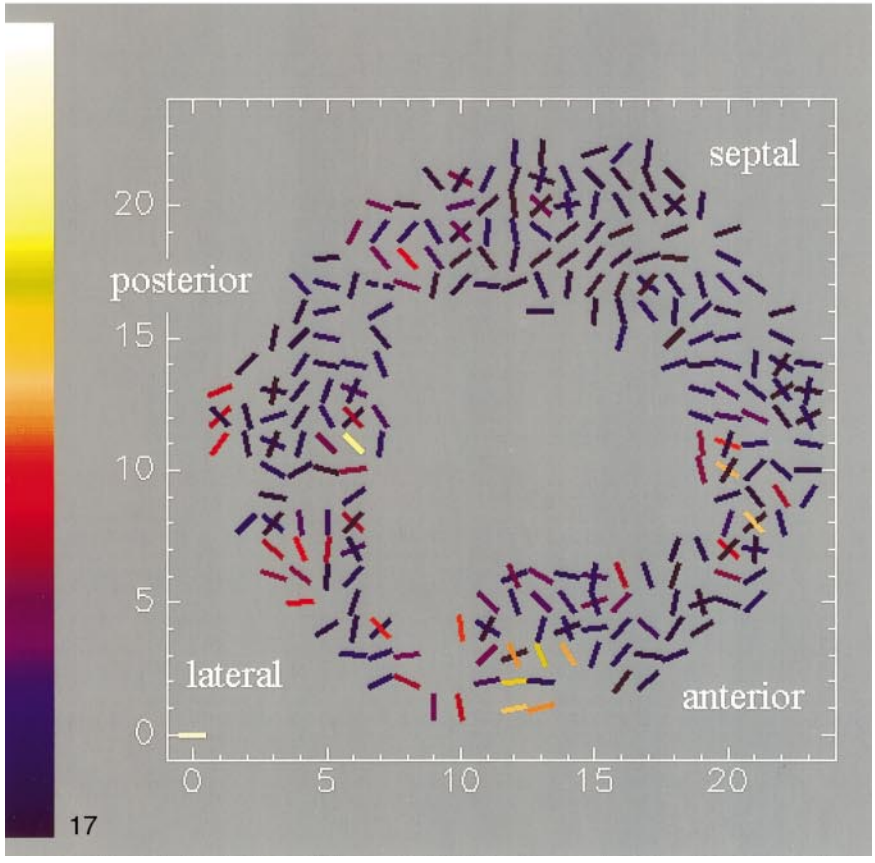
septal
posterior
lateral
anterior
0
5
10
15
20
17

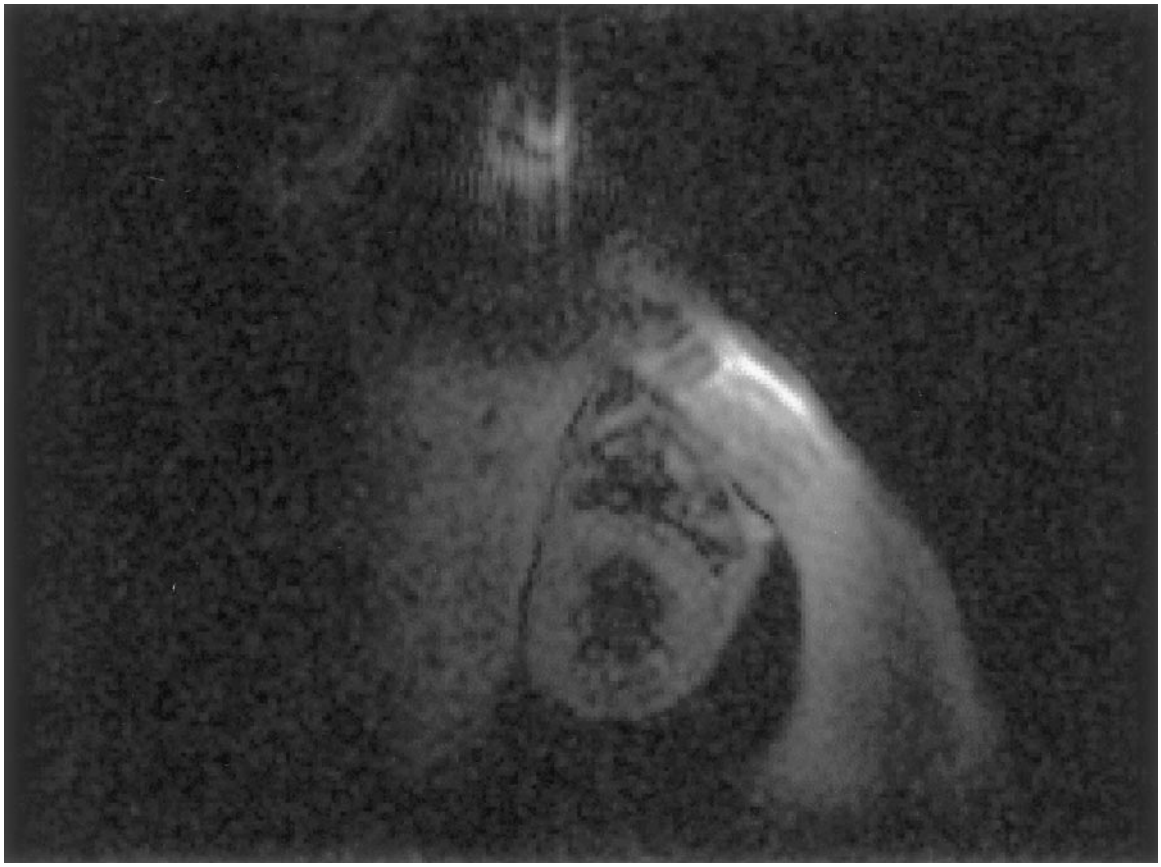

FIG. 18. Short-axis magnitude image of the human heart that demonstrates how X and Y slab selection can be utilized to attenuate signal originating from the periphery of the FOV.

come less significant when considering the overall phase dynamic range. Last, the acquisition process itself is through stimulated echoes that are in nature less susceptible to field inhomogeneity. Control data acquired with fast-DENSE from the human heart, as described under Methods, showed that the error in strain measurements is approximately 2.8%. In areas of the heart where the calculated strain falls below this noise level, the principal contraction and dilation directions tend to be random and do not reflect the actual muscle deformation.

It should be noted that in the normal heart, myocardial shortening is occurring along the fiber direction. Myocardial fibers of the left ventricle are oriented in a helical pattern, where the long axis of the helix is along the long axis of the heart. Therefore, DENSE data acquired with this 2D acquisition scheme sample the projection of the actual displacement onto the imaged slice. As such, the calculated circumferential strain is a weighted average of the strains along the circumference and the long axis.

The current implementation of fast-DENSE requires acquisition windows of 24 heartbeats. Even though this is adequate for normal volunteer exams, patient scans will need to be at least twice as fast. This may be feasible by recalling and imaging the STEAM-prepared magnetization via fast spin echo methods. We hope that such an approach will yield DENSE data of similar spatial resolution in 12 heartbeats in the future. Limiting fast-DENSE data to the last 100 ms of systole was also a result of the low flip angle imaging scheme. Fast spin

FIG. 16. Contraction strain map of the human heart over the last 105 ms of systole with Y encoding substituted by an additional reference scan (see text). The principal direction of contraction is shown via colored bars. Color scale represents 0 to 20% contraction. Average strain is 2.8% (SD = 2.5%) and represents the physiological noise level.

FIG. 17. Dilation strain map of the human heart over the last 105 ms of systole with Y encoding substituted by an additional reference scan (see text). The principal direction of dilation is shown via colored bars. Color scale represents 0 to 20% dilation. Average strain is 2.9% (SD = 2.5%) and represents the physiological noise level.

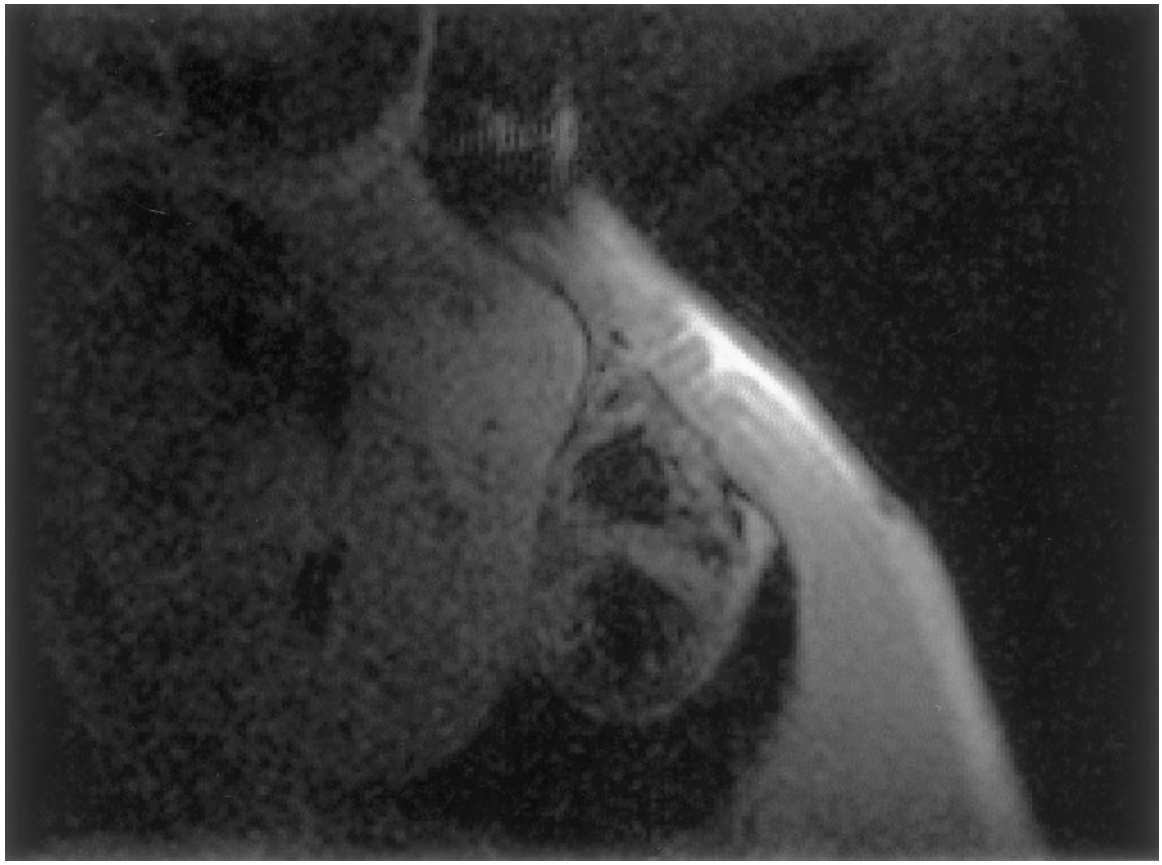

FIG. 19. Short-axis magnitude image of the human heart that demonstrates signal loss in the free left ventricular wall with increased TE gradient moment along the slice direction.

echo acquisition could provide the improved data SNR that can potentially allow strain analysis at high resolution over the full time course of systole.

CONCLUSIONS

We demonstrated that fast-DENSE can provide 2D strain maps from the human heart at 2.5 $\times$ 2.5 mm in-plane resolution with high precision in a 24-heartbeat breath-hold. Data processing is fast and requires little human interaction. Control experiments performed in normal volunteers yielded a noise level of 2.8 and 2.9% for circumferential and radial strains, respectively. Stationary phantom data showed that eddy currents and Maxwell terms induced an order of magnitude less noise than that detected under *in vivo* conditions. The principle of the method was verified via rotating phantom experiments.

REFERENCES

1. A. A. Young, C. M. Kramer, V. A. Ferrari, L. Axel, and N. Reichek, Three-dimensional left ventricular deformation in hypertrophic cardiomyopathy, *Circulation* **90,** 854–867 (1994).
2. A. A. Young, Z. A. Fayad, and L. Axel, Right ventricular midwall surface motion and deformation using magnetic resonance tagging, *Am. J. Physiol.* **271,** H2677–H2688 (1996).
3. A. A. Young, and L. Axel, Three-dimensional motion and deformation of the heart wall: Estimation with spatial modulation of magnetization—A model-based approach, *Radiology* **185,** 241–247 (1992).
4. P. M. Pattynama, A. De Roos, E. E. van der Wall, and A. E. Van Voorthuisen, Evaluation of cardiac function with magnetic resonance imaging. *Am. Heart J.* **128,** 595–607 (1994).
5. W. J. J. Rogers, E. P. Shapiro, J. L. Weiss, M. B. Buchalter, F. E. Rademakers, M. L. Weisfeldt, and E. A. Zerhouni, Quantification of and correction for left ventricular systolic long-axis shortening by magnetic resonance tissue tagging and slice isolation. *Circulation* **84,** 721–731 (1991).
6. E. R. McVeigh, Imaging asynchronous mechanical activation of the paced heart with tagged MRI. *Magn. Reson. Med.* **39,** 507–513 (1998).
7. M. Kass, A. Witkin, and D. Terzopoulos, Snakes: Active contour models. *Int. J. Comp. Vis.* **1,** 321–331 (1987).
8. P. R. Moran, A flow velocity zeugmatographic interlace for NMR imaging in humans. *Magn. Reson. Imaging* **1,** 197–203 (1982).
9. L. R. Pelc, J. Sayre, K. Yun, L. J. Castro, R. J. Herfkens, D. C. Miller, and N. J. Pelc, Evaluation of myocardial motion tracking with

cine-phase contrast magnetic resonance imaging. *Invest. Radiol.* **29,** 1038–1042 (1994).

10. N. J. Pelc, M. Drangova, L. R. Pelc, Y. Zhu, D. C. Noll, B. S. Bowman, and R. J. Herfkens, Tracking of cyclic motion with phase-contrast cine MR velocity data. *J. Magn. Reson. Imaging* **5,** 339–345 (1995).
11. R. T. Constable, K. M. Rath, A. J. Sinusas, and J. C. Gore, Development and evaluation of tracking algorithms for cardiac wall motion analysis using phase velocity MR imaging. *Magn. Reson. Med.* **32,** 33–42 (1994).
12. P. F. Castro, R. C. Bourge, and R. E. Foster, Evaluation of hibernating myocardium in patients with ischemic heart disease. *Am. J. Med.* **104,** 69–77 (1998).
13. T. G. Reese, V. J. Wedeen, and R. M. Weisskoff, Measuring diffusion in the presence of material strain, *J. Magn. Reson. B* **112,** 253–258 (1996).
14. A. E. Arai, C. J. Gaither, F. H. Epstein, R. S. Balaban, and S. D. Wolff, Myocardial velocity gradient imaging by phase contrast MRI with application to regional function in myocardial ischemia. *Magn. Reson. Med.* **42,** 98–109 (1999).
15. T. L. Chenevert, A. R. Skovoroda, M. O'Donnell, and S. Y. Emelianov, Elasticity reconstructive imaging by means of stimulated echo MRI. *Magn. Reson. Med.* **39,** 482–490 (1998).
16. A. H. Aletras, S. Ding, R. S. Balaban, and H. Wen, DENSE: Displacement encoding with stimulated echoes in cardiac functional MRI. *J. Magn. Reson.* **137,** 247–252 (1999).
17. M. A. Bernstein, M. Grgic, T. J. Brosnan, and N. J. Pelc, Reconstructions of phase contrast, phased array multicoil data. *Magn. Reson. Med.* **32,** 330–334 (1994).
18. E. McVeigh, Regional myocardial function. *Cardiol. Clin.* **16,** 189–206 (1998).
19. D. G. Wiesler, H. Wen, S. D. Wolff, and R. S. Balaban, Reduction of field of view in MRI using a surface-spoiling local gradient insert. *J. Magn. Reson. Imaging* **8,** 981–988 (1998).
20. P. Mills, W. Chew, L. Litt, and M. Moseley, Localized imaging using stimulated echoes. *Magn. Reson. Med.* **5,** 384–389 (1987).
21. J. P. Reilly, "Electrical Stimulation and Electropathology," Cambridge Univ. Press, Cambridge, UK (1992).
22. J. Frahm, W. Hanicke, H. Bruhn, M. L. Gyngell, and K. D. Merboldt, High-speed STEAM MRI of the human heart. *Magn. Reson. Med.* **22,** 133–142 (1991).
23. S. E. Fischer, M. Stuber, M. B. Scheidegger, and P. Boesiger, Limitations of stimulated echo acquisition mode (STEAM) techniques in cardiac applications. *Magn. Reson. Med.* **34,** 80–91 (1995).
24. V. J. Wedeen, MRI signal void due to in-plane motion is all-or-none. *Magn. Reson. Med.* **32,** 116–120 (1994).